

Radio Science®

RESEARCH ARTICLE

10.1029/2025RS008305

Key Points:

- Pre- t_0 phase technique for meteoroid speed determination using backscatter radar is extended to forward scatter continuous wave systems
- Integration of derived speeds improves trajectory reconstructions without interferometry, with 5% speed and 2–4° inclination errors
- Markov Chain Monte Carlo uncertainty quantification enables systematic and robust estimation of meteoroid trajectory parameters

Correspondence to:

J. Balis,
joachim.balis@aeronomie.be

Citation:

Balis, J., Lamy, H., Anciaux, M., Jehin, E., De Keyser, J., Kastinen, D., & Brown, P. G. (2025). Enhanced meteoroid trajectory and speed reconstruction using a forward scatter radio network: Pre- t_0 phase technique and uncertainty analysis. *Radio Science*, 60, e2025RS008305. <https://doi.org/10.1029/2025RS008305>

Received 8 APR 2025

Accepted 23 JUL 2025

Author Contributions:

Conceptualization: Joachim Balis, Hervé Lamy, Michel Anciaux, Emmanuel Jehin, Johan De Keyser, Daniel Kastinen, Peter G. Brown

Data curation: Joachim Balis

Formal analysis: Joachim Balis

Funding acquisition: Hervé Lamy, Johan De Keyser

Methodology: Joachim Balis, Hervé Lamy, Michel Anciaux, Emmanuel Jehin, Johan De Keyser, Daniel Kastinen, Peter G. Brown

Project administration: Hervé Lamy, Johan De Keyser

Resources: Hervé Lamy






Software: Joachim Balis, Daniel Kastinen

Supervision: Hervé Lamy, Emmanuel Jehin, Johan De Keyser, Peter G. Brown

© 2025. The Author(s).

This is an open access article under the terms of the [Creative Commons Attribution-NonCommercial-NoDerivs License](#), which permits use and distribution in any medium, provided the original work is properly cited, the use is non-commercial and no modifications or adaptations are made.

Enhanced Meteoroid Trajectory and Speed Reconstruction Using a Forward Scatter Radio Network: Pre- t_0 Phase Technique and Uncertainty Analysis

Joachim Balis^{1,2} , Hervé Lamy¹ , Michel Anciaux¹ , Emmanuel Jehin², Johan De Keyser¹ , Daniel Kastinen³ , and Peter G. Brown^{4,5}

¹Royal Belgian Institute for Space Aeronomy, Brussels, Belgium, ²STAR Institute, University of Liège, Liège, Belgium, ³Swedish Institute of Space Physics (IRF), Kiruna, Sweden, ⁴Department of Physics and Astronomy, Western University, London, ON, Canada, ⁵Institute for Earth and Space Exploration, Western University, London, ON, Canada

Abstract This study presents an enhanced method for reconstructing meteoroid trajectories and speeds using the Belgian RADio Meteor Stations forward scatter radio network. A novel extension of the pre- t_0 phase technique, originally developed for backscatter radars, has been adapted for forward scatter continuous wave systems. This method leverages phase data recorded before the meteoroid reaches the specular reflection point t_0 to improve speed estimations. Additionally, we combine this newly determined pre- t_0 speed information with time of flight measurements into the trajectory solver to reduce uncertainties in meteoroid path and speed reconstructions. A Markov Chain Monte Carlo method is employed to propagate measurement uncertainties to the trajectory parameters. The reconstructed trajectories and speeds are validated against optical data from the CAMS-BeNeLux network. The results show significant improvements in the accuracy and robustness of speed and inclination determination.

Plain Language Summary Meteoroids are small space rocks that enter Earth's atmosphere, creating bright streaks of light known as meteors. Understanding their speed and path helps scientists and engineers learn more about where they come from and how much of a hazard they pose to satellites. This study improves the way we measure meteoroid speeds using a network of radio stations in Belgium called Belgian RADio Meteor Stations. We apply a new technique that analyzes the phase of the radio signal before the meteoroid reaches the optimal reflection point. We combine this new method with advanced algorithms to retrieve the meteoroid's path more accurately. The results are compared with camera observations and show improved precision in terms of speed and inclination.

1. Introduction

The determination of meteoroid trajectories and speeds in Earth's atmosphere is essential for various scientific and engineering purposes. They are essential inputs for determining meteoroid pre-impact orbits and thus better understanding the dynamics and evolution of small bodies in our Solar System (Ceplecha, 1987). From a science perspective, meteoroid orbital information constrains the modeling of dust deposited by meteoroids in Earth's atmosphere (Carrillo-Sánchez et al., 2016). For engineering purposes, knowledge of the trajectories and speeds of meteoroids are crucial to assess the impact risk with spacecraft (Soja et al., 2019).

Radio meteor measurement techniques offer several advantages over their optical counterparts. First, they are sensitive to much smaller particles. This is particularly relevant because of the size distribution of meteoroids: these small objects bring most of the mass influx to Earth (Ceplecha et al., 1998). Second, radar works at night and under bad weather conditions. Meteor radars usually study the specular scattering from meteor ionized trails, rather than head echoes. The latter, caused when radio waves are reflected from the immediate plasma surrounding the meteoroid, have a smaller radar cross section and therefore require more transmit power for detection. For this reason, head echoes are usually studied using high-power large aperture radars (W. Baggaley, 2009).

The nature of the scattering on a meteoroid trail depends on the electron volume density of the ionized trail. If the electron density is low enough that the incoming radio wave penetrates the trail and each free electron responds individually to the wave's electric field, the reflection is said to be underdense. In contrast, when the electron

Validation: Joachim Balis, Hervé Lamy, Michel Anciaux, Emmanuel Jehin, Johan De Keyser, Daniel Kastinen, Peter G. Brown

Visualization: Joachim Balis, Daniel Kastinen

Writing – original draft: Joachim Balis

Writing – review & editing:

Joachim Balis, Hervé Lamy, Michel Anciaux, Emmanuel Jehin, Johan De Keyser, Daniel Kastinen, Peter G. Brown

density is high enough to reflect the radio wave as from a metallic surface, the trail is called overdense (McKinley, 1961). Trails that fall in between these two regimes are referred to as transitional.

There exist many independent single-station speed measurement techniques. Most approaches for determining speed from the radio wave scattering off a meteor trail are based on the Fresnel diffraction theory applied to a half-plane (McKinley, 1961). The simplest technique is called “pre- t_0 amplitude” or rise-time approach and is based on measurements of the rise-time of the radar received time-amplitude profile before the passage of the meteoroid at the specular point t_0 . However, this method has shown to deteriorate quickly at low signal-to-noise ratios (SNRs) and to provide less accurate speed estimates compared to other techniques (Baggaley et al., 1997).

The oldest method is named “post- t_0 amplitude” or fresnel amplitude oscillation speed measurement approach (Ellyett & Davies, 1948; McKinley, 1961). In this technique, the amplitude time series after the point of maximum amplitude is examined. Oscillations due to the Fresnel diffraction pattern are analyzed and the meteoroid speed is inferred from their frequency. Despite being more accurate than the pre- t_0 amplitude method, it is only applicable to the minority of echoes that do not show signs of fragmentation, that is, no break-up of the meteoroid in smaller pieces (Elford & Campbell, 2001).

The most recent method is called the Fresnel Transform (FT), an approach that utilizes both the phase and amplitude associated with the radio echo of a meteor (Elford, 2004). Although this technique was initially introduced to study the structure of the ionized trail behind the head of the meteor, in practice the FT has been used mainly to calculate meteoroid speed. While this approach usually has the smallest speed uncertainties, it is computationally the most costly. Moreover, it is not straightforward to automate, as shown by the various techniques described in the literature (W. J. Baggaley & Grant, 2005; Campbell & Elford, 2006; Holdsworth et al., 2007; Roy et al., 2007).

Finally, the last radar single-station speed measurement method that has been widely used is the “pre- t_0 phase” approach, first presented by Cervera et al. (1997). As its name suggests, it relies on the phase profile before the specular point t_0 and is therefore much less affected by potential deterioration of the speed measurement due to fragmentation. Compared to other approaches, it has been shown to work well at lower echo SNR and produce useable speeds for most echoes. Moreover, recent automation techniques have been introduced to exploit this method for backscatter radars (Mazur et al., 2020).

In a previous paper (Balis et al., 2023), we solved for the first time the challenge of reconstructing meteoroid trajectories using a forward-scatter radio system transmitting a continuous wave (CW) without modulation. Our method relied on measuring and comparing the times of passage at the t_0 points, as observed by multiple spatially separated receivers of the Belgian RADio Meteor Stations (BRAMS) network. We demonstrated the ill-conditioned nature of the problem. We showed that the solution strongly depends on the quality of the measurements. If additional information from an interferometer is available, the conditioning of the problem strongly improves.

In this paper, we aim to improve our trajectory reconstructions with BRAMS without using interferometry. We introduce the BRAMS network and its technical specifications in Section 2. In Section 3, we extend the pre- t_0 phase approach for speed measurements to a forward scatter CW system. In Section 4, we tackle the systematic characterization of uncertainties on t_0 measurements and pre- t_0 speeds. We also integrate the extra speed information contained in pre- t_0 phases into our trajectory solver. In Section 5, we adapt a Markov-Chain Monte Carlo (MCMC) method originally developed by Kastinen and Kero (2022) to propagate the measurement uncertainties to our trajectory parameters. In Section 6, we compare our reconstructed trajectories with optical data provided by the CAMS-BeNeLux network (Jenniskens et al., 2016). We end with a conclusion and a discussion of future research directions.

2. BRAMS Network

BRAMS possesses a dedicated transmitter in Dourbes (south of Belgium) that emits a circularly polarized continuous radio wave with no modulation at a frequency of 49.97 MHz. In 2024, the transmitted power was increased from about 130 W to approximately 350 W.

The 50 receiving stations each use a three-element vertical Yagi antenna oriented in azimuth toward the transmitter. As of February 2025, the majority of receivers use digital software-defined radio (SDR) receivers

controlled by a Linux system running on a Raspberry Pi (Anciaux et al., 2020) or a ROCK4 Starter Edition. A handful of receiving stations still use analog ICOM-R75 receivers, an external sound card to sample the signal coming from the antenna, and are controlled by the freeware Spectrum Lab program running on a PC (Lamy et al., 2015). These stations are being progressively replaced by the more modern SDR receivers, which provide higher sensitivity and wider dynamic range.

At the receiving stations, the signal is downshifted to 1,000 Hz and is then sampled at 6,048 Hz for the SDR systems and at 5,512 Hz for the ICOM. All stations are equipped with a Garmin GPS that provides timestamps with microsecond-level accuracy to the BRAMS data. This allows for a time synchronization between the receiving stations, which is necessary for the determination of the times of flight (TOF) between the detections of different specular reflections along the same trail.

A 6-antenna radio interferometer located in Humain, 50 km away from the transmitter, provides the angle of arrival of one specular point. This system uses AR5001D analog receivers in conjunction with 16-bit simultaneous samplers (NI 9215) controlled by a Labview program running on a dedicated PC.

For further information about the specifications of the BRAMS network, we refer the reader to previous publications (Anciaux et al., 2020; Lamy et al., 2015).

3. Pre- t_0 Phase

3.1. General Theory for a Backscatter Radar System

As discussed by McKinley (1961), \mathcal{F}_{\sin} and \mathcal{F}_{\cos} are the Fresnel integrals defined by:

$$\begin{aligned}\mathcal{F}_{\sin} &= \int_{-\infty}^{x(t)} \sin\left(\frac{\pi}{2}u^2\right) du, \\ \mathcal{F}_{\cos} &= \int_{-\infty}^{x(t)} \cos\left(\frac{\pi}{2}u^2\right) du,\end{aligned}\tag{1}$$

where x is the dimensionless Fresnel parameter along the spiral formed by the parametric plot of the Fresnel integrals. The power reflected by an underdense meteor echo is proportional to $\mathcal{F}_{\sin}^2 + \mathcal{F}_{\cos}^2$.

A plot of \mathcal{F}_{\sin} as a function of \mathcal{F}_{\cos} gives the Cornu spiral, which is useful to describe the amplitude and phase variation of the meteor echo, as illustrated in Figure 1. In the top panel, the distance between the starting point (where $x = -\infty$ and where $\mathcal{F}_{\sin} = \mathcal{F}_{\cos} = -0.5$) and the current location on the Cornu spiral gives the theoretical amplitude of the meteor echo. Similarly, the angle between the horizontal line and the vector joining the starting point and the current location on the Cornu spiral gives the theoretical phase of the meteor echo. The amplitude and phase behaviors as a function of x are plotted on the bottom panel of Figure 1, along with some characteristic points.

The pre- t_0 phase method was introduced by Cervera et al. (1997) for backscatter radars, and later refined and automated by Mazur et al. (2020). This technique uses the phase curve of Figure 1 to retrieve the speed of the meteoroid. After phase extraction from the radio data, each sample is associated to a given value of the Fresnel parameter x thanks to the Cornu spiral model. Then, this parameter is converted to the distance along the trail s for backscatter radars:

$$s = \frac{\sqrt{R\lambda}}{2}x,\tag{2}$$

where s is the distance along the trail, R is the range of the echo from the station and λ is the radar wavelength. Provided stations are absolutely synchronized in time (such as via GPS timestamps) the timing difference in echo occurrence can be used to obtain a curve $s(t)$ of the distance along the trail as a function of time. The slope of this curve gives an estimate of the meteoroid velocity $v(t)$. Note that this approach explicitly ignores deceleration and assumes a constant velocity across all Fresnel zones.

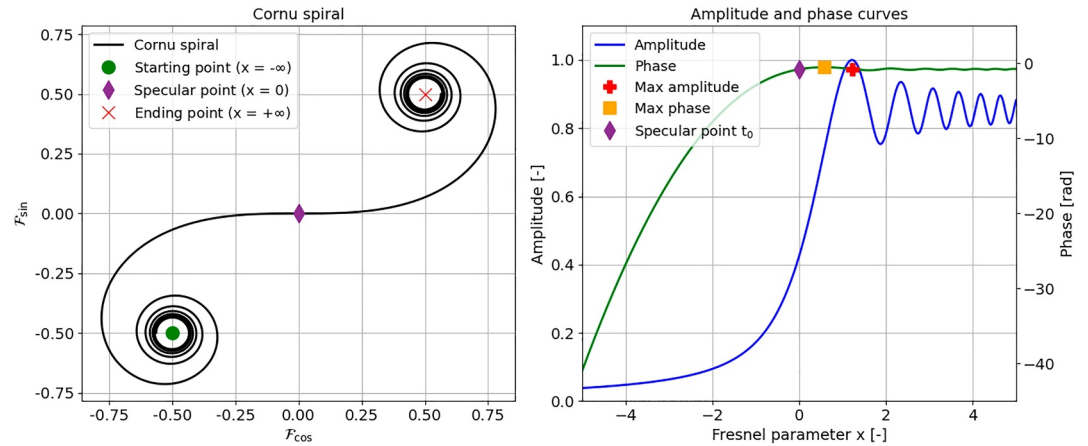


Figure 1. Cornu spiral and corresponding amplitude and phase curve. Left panel: the spiral and its characteristic points. The green circle indicates the start of the spiral (in $x = -\infty$), the purple diamond is the passage at the specular point ($x = 0$), and the red cross is the end of the spiral (in $x = +\infty$). Right panel: amplitude and phase variation with the Fresnel parameter x . The points corresponding to maximum amplitude and maximum phase are plotted on the phase curve. Physically a phasor with its origin at $x = -\infty$ represents the signal at the receiver as the meteor moves along a path perpendicular to the radar line of site. The Cornu spiral starts at $x = -\infty$ when the meteor is far from the specular point and the phasor head moves along the spiral as the meteor transits through the specular point. Here x is a range and wavelength scaled distance.

While Cervera et al. (1997) provide some general considerations about the pre- t_0 approach, Mazur et al. (2020) introduced a detailed operational method of measuring pre- t_0 speed from radar data via a sliding-slopes technique (PSSST). This approach aims to estimate reliable speeds and associated uncertainties.

More specifically, after extraction of the phase curve and removal of the wind drift through system-specific processing, the t_0 point is identified. This point is determined by moving back in time pulse by pulse from the point of maximum amplitude, passing by the point of maximum phase and then identifying the specular point (respectively the red cross, the yellow square and the purple diamond in Figure 1).

Then, an analysis region is chosen around the t_0 point, within which the $s(t)$ curve is segmented using multiple sliding windows of varying sizes. A linear fit is performed on each of these windows, leading to a histogram of slopes. The latter is then fitted by a weighted Kernel Density Estimator (KDE), whose maximum gives an estimation of the speed. Its related uncertainty is based on the full width at half maximum (FWHM) of the fitted distribution. More information about this process can be found in Mazur et al. (2020).

3.2. Extension to Forward Scatter

We aim to extend the pre- t_0 phase method to forward scatter systems such as BRAMS. To do so, we generalize Equation 2 to a general radio set-up:

$$s = \frac{\sqrt{2}d_f}{2}x, \quad (3)$$

where d_f is the length of the first Fresnel zone. The exact expression of d_f depends on the type of radio propagation system. For backscatter systems, $d_f = \sqrt{2R\lambda}$ such that we retrieve Equation 2. For forward scatter systems, we have (Wislez, 2006):

$$d_f = 2\sqrt{\frac{\lambda R_T R_R}{(R_T + R_R)(1 - \sin^2 \phi \cos^2 \beta)}}, \quad (4)$$

where R_T is the distance from the transmitter to the meteor specular point and R_R is the distance from the specular point to the receiver. Here ϕ is the half forward scatter angle and β is the angle between the meteoroid trajectory

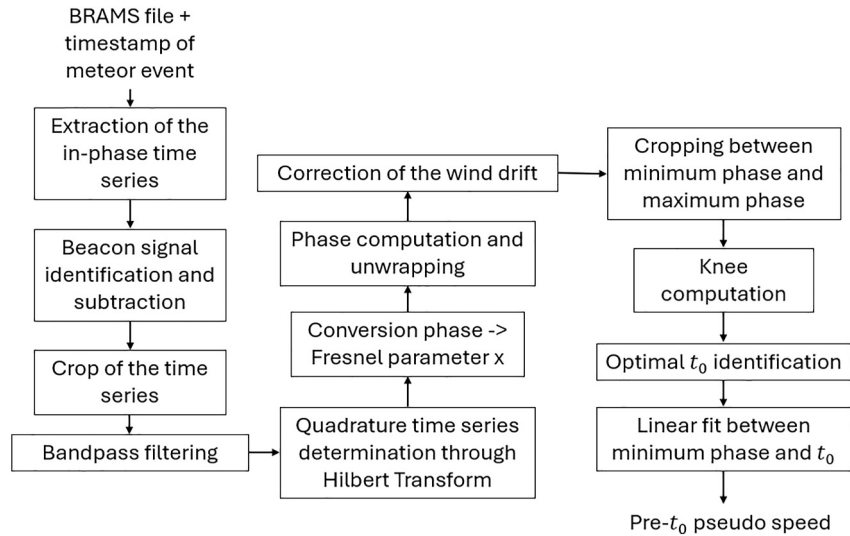


Figure 2. Workflow for the pre- t_0 speed extraction with Belgian RAdio Meteor Stations.

and the propagation plane. Setting $R_T = R_R = R$ and $\phi = 0^\circ$ leads to the same expression as in backscatter systems.

The corresponding pre- t_0 speed will then be simply defined as the derivative of Equation 3 with respect to time, that is:

$$v = \frac{\sqrt{2}d_f}{2} \frac{dx}{dt}. \quad (5)$$

In contrast with radars such as the Canadian Meteor Orbit Radar (CMOR) which measure range to an echo (Jones et al., 2005), BRAMS receivers do not provide any range information. Therefore, the geometry parameters appearing in Equation 5 are not available during the processing. As a result, we introduce a pre- t_0 pseudo speed, i.e. $\frac{dx}{dt}$. The addition of the geometry information will be discussed in Section 4.

The processing of the BRAMS signals for the pre- t_0 phase extraction is extended from the initial algorithm presented by Balis et al. (2023). The main steps are illustrated in Figure 2 and detailed hereafter.

From the raw amplitude obtained at the receiving stations, we identify the beacon signal and subtract it. An example of the resulting spectrogram is given in panel (a) of Figure 3.

We then extract an interval of 5 s around the meteor echo and identify the frequency of the meteor f_m which has the highest power spectral density. This frequency corresponds to the sum of a modulation at 1,000 Hz and the Doppler effect due to wind drift. Finally, we apply a filter with a bandpass of 600 Hz around f_m to extract only the information relevant to the meteor and to increase the SNR. The resulting amplitude curve is given in panel (b) of Figure 3.

With BRAMS, both the SDR and the analog receivers only preserve the i (in-phase) component. Therefore, we determine the q (quadrature) component analytically through a Hilbert transform of the i component. Once both q and i components are available, the phase is computed with $\phi = \arctan(\frac{q}{i})$. Finally, after phase unwrapping, the modulation due to the meteor frequency f_m is subtracted through $\phi_{corr} = \phi - 2\pi f_m t$ where t is the time vector. This leads to the phase curve given in panel (c) of Figure 3.

A properly defined analysis region needs to be identified on the phase curve for speed determination. To do so, we crop the phase curve from the point of a sufficiently pronounced phase minimum until the point of maximum amplitude, as illustrated in panel (d) of Figure 3. Heuristically, we determined that the phase minimum should have at least a prominence of 1 radian. We also impose that it be located after the fourth Fresnel zone from the t_0 point. This corresponds to a phase minimum with a value smaller than ≈ -14 radians. Otherwise, the

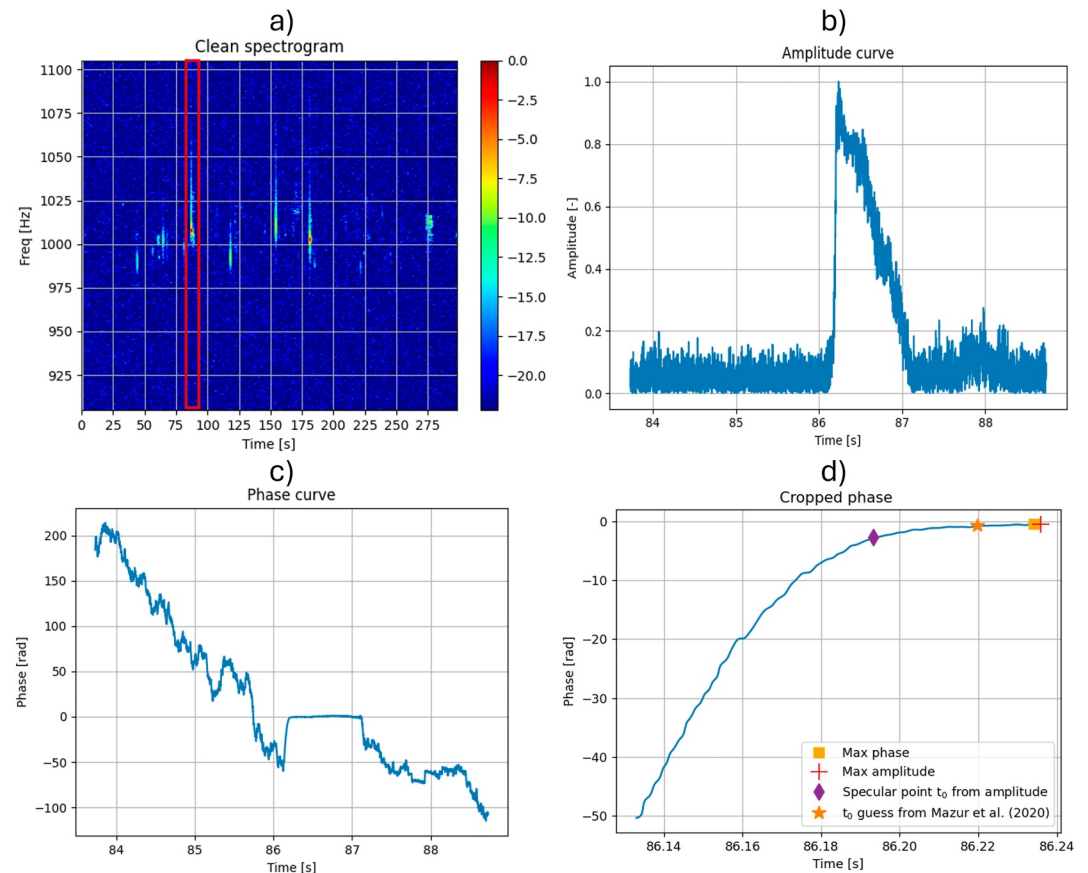


Figure 3. Phase information extraction from Belgian RADIo Meteor Stations data. (a) Spectrogram after beacon subtraction. The power is color-coded in dB FS (Decibels relative to Full Scale). The red rectangle highlights the meteor of interest. (b) Amplitude of the meteor echo obtained after bandpass filtering. (c) Phase of the meteor echo obtained after bandpass filtering and wind drift subtraction. The green rectangle is the part of the phase curve used for pre- t_0 speed computation. (d) Zoom on the green rectangle of panel (c).

corresponding echo is rejected. The criterion of 4 Fresnel zones comes from the necessity to have enough points to retrieve accurate speed information.

In this region of the phase curve, it appears that the “moving back in time” method proposed by Mazur et al. (2020) is not ideal for BRAMS, even at high SNR. Indeed, we can see in the panel (d) of Figure 3 that the determination of the t_0 point with this approach is quite far from the t_0 guess determined from the amplitude curve. Instead, we convert the determined phases to Fresnel parameters through the model of the Cornu spiral. In these new coordinates, we look at the knee of the curve. As we can see in the panel (a) of Figure 4, the knee is relatively close to the specular point determined with the amplitude curve.

The determination of the knee is however not enough for accurate pre- t_0 speed determination. Indeed, the necessity to determine an accurate t_0 point on the phase curve is a critical component to obtain a reliable pre- t_0 speed. Mazur et al. (2020) suggested to refine the t_0 guess after its automatic determination to increase the accuracy of their PSSST algorithm. The authors proposed to drive this refinement by a minimization of the width of the KDE but never implemented this feature.

Here, we decide to start from the knee as an initial t_0 value. We then perturb this assumed t_0 sample by sample. For each guess, we perform a linear fit on the $x(t)$ curve between the minimum phase point and the current t_0 guess. The slope of the linear fit which shows the highest coefficient of correlation r is taken as our pre- t_0 pseudo speed. The example of this best linear fit and its associated pre- t_0 pseudo speeds are given in the panel (b) of Figure 4.

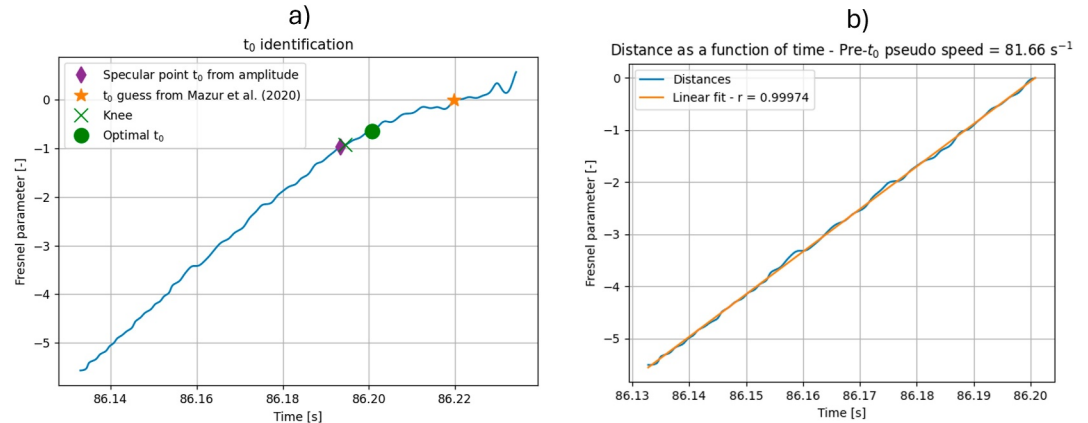


Figure 4. Pre- t_0 pseudo speed information extraction from Belgian Radio Meteor Stations data. (a) Determination of the knee and optimal t_0 on the $x(t)$ curve. (b) Linear fit on the optimal $x(t)$.

Our approach of using the pre- t_0 pseudo speed information provides two important benefits. First, it provides a systematic way to find the t_0 timing, which is necessary for the computation of the TOF. Secondly, it brings new information for the trajectory reconstruction process. In the following sections, we describe how we incorporate these additional inputs into the trajectory solver.

4. Solver Improvement

A meteoroid trajectory can be defined by the 3D Cartesian coordinates of one specular point (the one corresponding to a reference station) and the three components of the velocity which provide the direction (assuming a constant speed). This gives a total of six unknowns (respectively called X_0 , Y_0 , Z_0 , V_x , V_y and V_z).

In Balis et al. (2023), we solved this problem of reconstructing meteoroid trajectories using a CW forward scatter system without modulation such as BRAMS. To do so, we input the TOF between several receivers into a non-linear cost function. While solvable, this problem is highly ill-conditioned, meaning that the accuracy of the solution is strongly dependent on measurement quality. As a result, reliable solutions were mostly obtained with the addition of interferometry measurement. However, this approach is only applicable for the minority of meteors which are detected by the interferometer in Humain.

In order to solve the trajectory problem without interferometry, we introduce a new cost function to minimize, incorporating information from both TOF and pre- t_0 phase curve:

$$L = \sum_{i=1}^n \left(\frac{\Delta t_{i,obs} - \Delta t_{i,model}}{\sigma_{\Delta t_{i,obs}}} \right)^2 + \sum_{j=1}^m \left(\frac{v_{j,pt0} - v_{j,model}}{\sigma_{v_{j,pt0}}} \right)^2, \quad (6)$$

where $\Delta t_{i,obs}$ is the experimental time of flight measured between a station i and a reference station, while $\Delta t_{i,model}$ is a time of flight coming from the forward trajectory reconstruction problem. $v_{j,pt0}$ is the experimental pre- t_0 speed measured at a receiver j while $v_{j,model}$ is the norm of the velocity and is equal to $\sqrt{V_x^2 + V_y^2 + V_z^2}$. $\sigma_{\Delta t_{i,obs}}$ and $\sigma_{v_{j,pt0}}$ are the uncertainties respectively on the time of flight at station i and on the pre- t_0 speed at station j . Their determination are the subject of Section 4.1. In Equation 6, one station can provide both a time of flight and a pre- t_0 phase.

This problem is solved iteratively using a Sequential Least Squares Programming solver (Kraft, 1988) in Python. In this approach, v_{pt0} is computed at each iteration through a rewriting of Equation 5:

$$v_{pt0} = K \sqrt{\frac{\lambda}{2}} \frac{dx}{dt}, \quad (7)$$

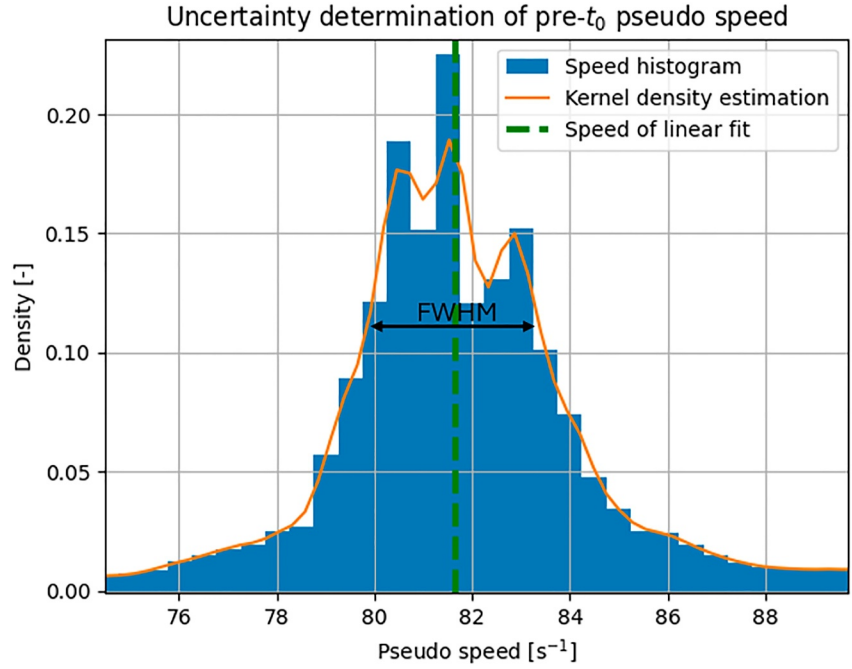


Figure 5. Full width at half maximum determination used in the computation of $\sigma_{\frac{dx}{dt}}$ following the PSSST approach.

where $K = \sqrt{\frac{R_T R_R}{(R_T + R_R)(1 - \sin^2 \phi \cos^2 \beta)}}$ is computed based on the assumed solution at a given iteration, while the pseudo speed $\frac{dx}{dt}$ is obtained for data from the analysis approach described in Section 3.

4.1. Input Uncertainty

4.1.1. Pre- t_0 Speed Uncertainty

The pre- t_0 speed uncertainty we use is an adaptation of the heuristic PSSST approach presented by Mazur et al. (2020). The uncertainty determination requires first the knowledge of the optimal t_0 and the corresponding pre- t_0 speed. The latter are determined by the identification of the optimal linear fit on the $x(t)$ curve, as discussed in Section 3.

To find the optimal t_0 position, an analysis region with an extension of Y samples is then isolated. There, sliding segments of lengths $L \in [2, Y]$ are considered. On each of these segments, a linear fit is performed on the $x(t)$ curve and the corresponding slope is extracted, similar to the procedure shown in Figure 4.

This process leads to a histogram of pseudo speeds $\frac{dx}{dt}$, as shown in Figure 5. A gaussian-based KDE is then fit to the pseudo speed histogram. The FWHM of the determined KDE is finally used as a characterization of the uncertainty: we assume a normal-like distribution and compute $\sigma_{\frac{dx}{dt}} = \frac{\text{FWHM}}{2\sqrt{2 \ln(2)}}$.

This uncertainty is converted in proper speed dimensions during each solver iteration, using a relation similar to Equation 7:

$$\sigma_{v_{pt0}} = K \sqrt{\frac{\lambda}{2}} \sigma_{\frac{dx}{dt}}. \quad (8)$$

4.1.2. Time of Flight Uncertainty

Assuming independent measurements between receivers, we have for the i th receiver an uncertainty given by:

$$\sigma_{\Delta t_{i,obs}} = \sqrt{\sigma_{t_{0,i}}^2 + \sigma_{t_{0,ref}}^2}. \quad (9)$$

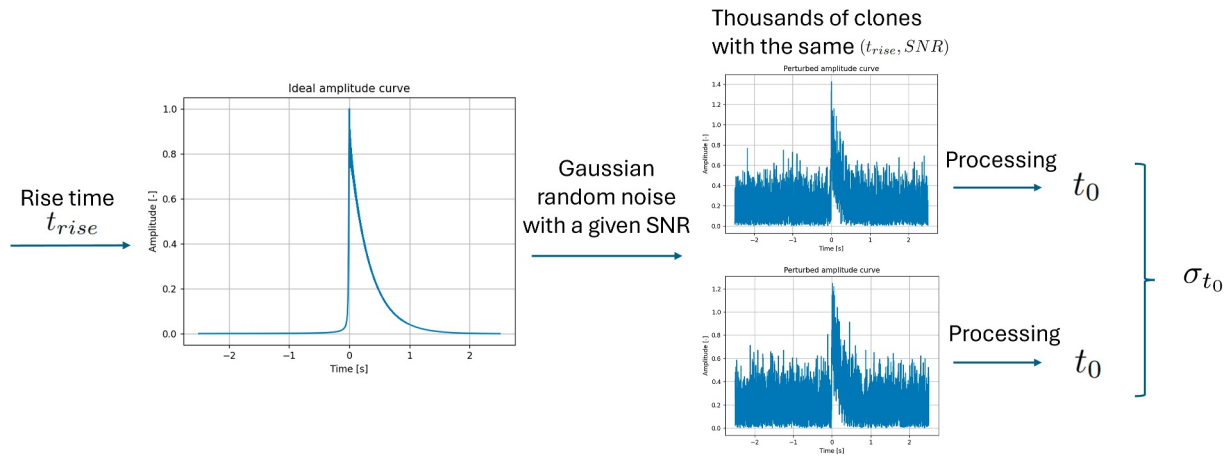


Figure 6. Workflow for the determination of σ_{t_0} through Direct Monte Carlo using synthetically generated meteor echoes.

The uncertainty on the time of flight can therefore be obtained by the uncertainty on the specular timing identification σ_{t_0} on a given receiver i and on the reference station. Here, we characterize this uncertainty in a similar way as done by Weryk and Brown (2012) for CMOR. In their work, the trajectory reconstruction problem with interferometry is solved and, given the solution (speed, radiant, azimuth, range), a model of an underdense meteor echo is generated. Knowing the SNR of the measured event, a large number of Monte Carlo clones are created and the trajectory solver is called with perturbed inputs. Statistics on the output can then be obtained.

In our case, the problem is different because we need to have access to the measurement uncertainties before solving for the trajectory. Indeed, the cost function (shown in Equation 6), which is used to reconstruct the meteoroid trajectory and the speed, requires the knowledge of σ_{t_0} .

To accomplish this, we determine a function such that:

$$\sigma_{t_0} = f(t_{\text{rise}}, \text{SNR}), \quad (10)$$

where t_{rise} is a measure of a rise time on the meteor amplitude curve. To find a proper rise time metric, let us recall that the specular point is located at the center of the first Fresnel zone. Hence, its uncertainty σ_{t_0} is mainly driven by the dynamics of the meteor echo in that region. A trade-off has to be made because very short rise times will be affected by oscillations in the noise. As a result, we decided it was more robust to characterize the rise time as the duration that the echo takes to cross the central 20% of the first Fresnel zone.

The function was determined through Direct Monte Carlo (DMC) sampling. As illustrated in Figure 6, combinations of various values of t_{rise} and SNR are modeled. For each modeled rise time, an ideal meteor echo is generated through the Fresnel integrals given in Equation 1. A constant diffusion time $\tau = 0.5$ s is added to the model. For each SNR, 10,000 clones of this echo are taken and a Gaussian noise time series is added to each of them separately. Then, the specular point time is determined on every noisy echo using the same post-processing chain as for actual echoes. Finally, the output statistics σ_{t_0} are drawn from this synthetic population.

Results of the DMC simulation process are given in Figure 7. The latter shows the large uncertainty increase as the SNR is decreased. This corroborates our earlier the approach that we initially introduced in (Balis et al., 2023), where we weighted our cost function inversely with the SNR.

Another clear trend is the increase of the uncertainty with the increase of the rise time, for a constant SNR. Hence, a meteoroid which takes longer to cross the first Fresnel zone will tend to have a less accurately measured specular point. This can happen because the meteoroid is either slow or the first Fresnel zone is long. Looking at Equation 4, the difficulty in accurately determining the timings t_0 will therefore be particularly challenging in the following cases:

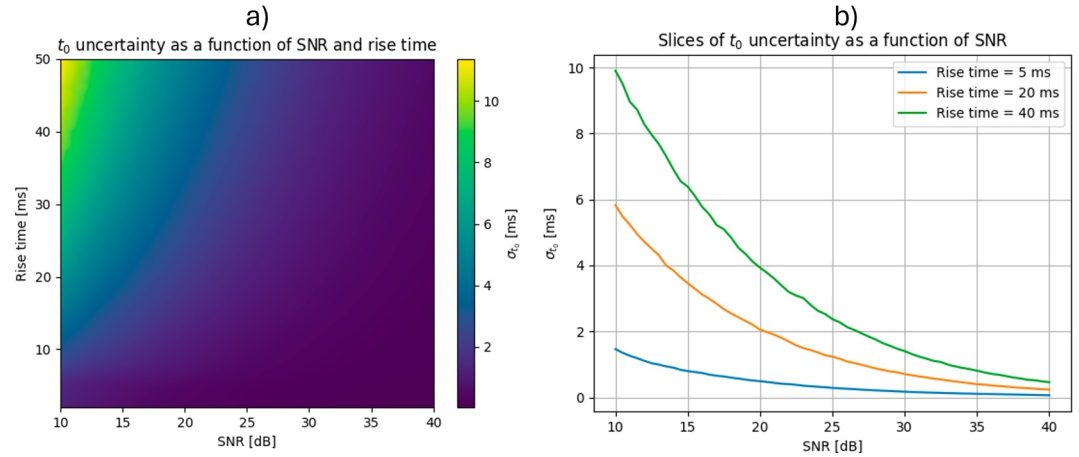


Figure 7. Results of the Direct Monte Carlo simulations showing σ_{t_0} . (a) Interpolated color map of the uncertainty as a function of signal-to-noise ratios (SNR) and rise time. (b) Slices of the specular timing uncertainties as a function of the SNR for various rise times.

- The meteoroid is far from the transmitter and the receiver, i.e. R_T and R_R are large.
- The receiver and the transmitter are far from each other, i.e. ϕ is close to 90° .
- The meteoroid moves in the wave propagation plane, i.e. β is close to 0° .

4.2. Pareto Front

As shown in Equation 6, we now have two different terms in the cost function, one linked to the TOF and one linked to the pre- t_0 speeds. These two terms drive the cost function in different directions as the reduction of the error in one will usually lead to the increase of the error in the other. This situation is typical of multi-objective optimization problems.

The measurement uncertainties in the denominator of Equation 6 aim to make the relative contribution of each term comparable. Yet, it can be interesting to come up with an approach allowing us to find a solution that would be “ideal,” in the sense that it would find the best compromise between the two objectives.

For this reason, we introduce a weighted cost function:

$$L = (1 - w) \sum_{i=1}^n \left(\frac{\Delta t_{i,obs} - \Delta t_{i,model}}{\sigma_{\Delta t_{i,obs}}} \right)^2 + w \sum_{j=1}^m \left(\frac{v_{j,p0} - v_{j,model}}{\sigma_{v_{j,p0}}} \right)^2, \quad (11)$$

where w varies between 0 and 1. When $w = 0$, we retrieve the time of flight solution. Equation 11 can be rewritten as:

$$L = (1 - w)L_{tof} + wL_{pt0}. \quad (12)$$

Evaluating Equation 12 for various weights lead to the creation of a Pareto front, that is, the set of all the optimal solutions, as illustrated in Figure 8. This curve represents the pre- t_0 cost function L_{pt0} plotted against the time-of-flight cost function L_{tof} at convergence for different values of the weight w . There exist various criteria in the literature to choose a solution from the Pareto front (Rao & Lakshmi, 2021; Wang & Rangaiah, 2017). Here, we settle for an identification of the knee of the Pareto front in a log-log representation, through an estimation of the point of maximum curvature (Aster et al., 2019; Hansen, 1992).

We note that the weighted cost function in Equation 11 is similar to the following cost function:

$$L = \sum_{i=1}^n \left(\frac{\Delta t_{i,obs} - \Delta t_{i,model}}{\hat{\sigma}_{\Delta t_{i,obs}}} \right)^2 + \sum_{j=1}^m \left(\frac{v_{j,p0} - v_{j,model}}{\hat{\sigma}_{v_{j,p0}}} \right)^2, \quad (13)$$

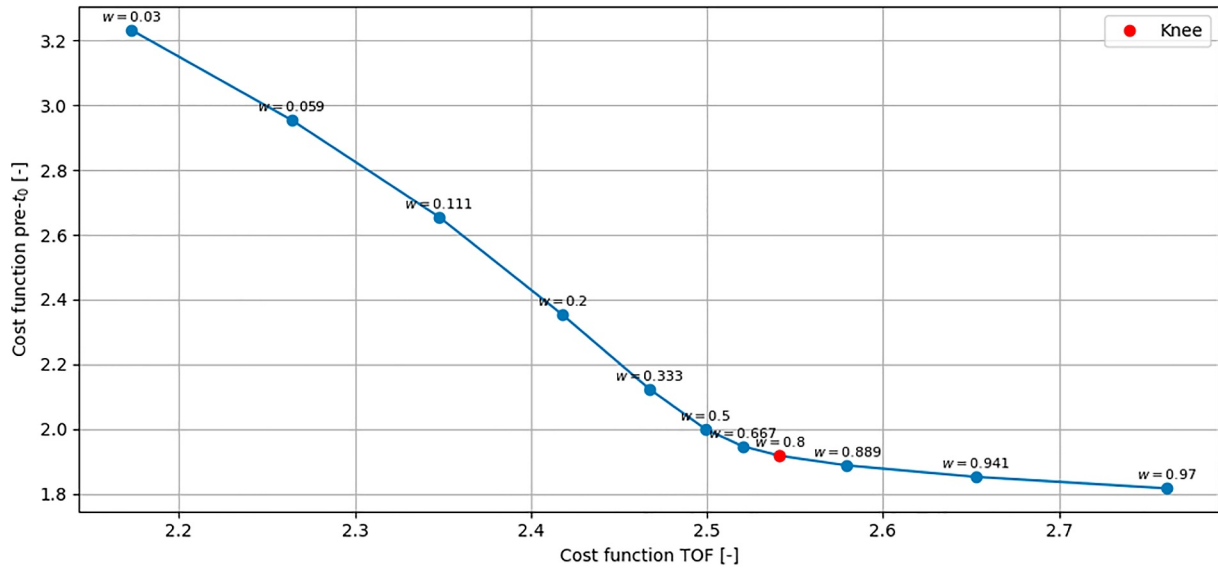


Figure 8. Log-log representation of the Pareto front and identification of the knee (red point).

with inflated uncertainties $\sigma_{\Delta t_{i,obs}} = \frac{\sigma_{\Delta t_{i,obs}}}{\sqrt{1-w}}$ and $\hat{\sigma}_{v_{j,p0}} = \frac{\sigma_{v_{j,p0}}}{\sqrt{w}}$.

While the uncertainties on the specular point timings and the pre- t_0 speeds have been quantified in as physically a realistic manner as possible respectively by DMC simulations and by KDE fitting, they might sometimes not characterize the measurement perfectly. An example is the determination of the uncertainty on the specular point timing for a transitional or overdense meteor echo. In that case, the assumption of underdense reflection used during the DMC simulations will potentially lead to underestimated σ_{t_0} .

To correct for these underestimations, we can use the residuals at the converged solution. If the problem is well-dimensioned and the uncertainties are meaningful, we would expect the dimensionless residuals to be of the order of 1. Therefore, we compute the following terms at the converged solution:

$$\alpha_{\Delta t} = \sqrt{\frac{1}{n} \sum_{i=1}^n \left(\frac{\Delta t_{i,obs} - \Delta t_{i,model}}{\hat{\sigma}_{\Delta t_{i,obs}}} \right)^2}, \quad (14)$$

$$\alpha_{p0} = \sqrt{\frac{1}{m} \sum_{j=1}^m \left(\frac{v_{j,p0} - v_{j,model}}{\hat{\sigma}_{v_{j,p0}}} \right)^2}.$$

If any of these terms are higher than 1, the corresponding uncertainties in the denominator are underestimated. In such a case, we rescale the $\hat{\sigma}$ by multiplying them with the corresponding α . In particular, in the case of transitional or overdense echoes, it often happens that $\alpha_{\Delta t}$ is greater than 1 so that the corresponding $\hat{\sigma}_{\Delta t_{i,obs}}$ must be increased before proceeding with the uncertainty estimation of the solution described in Section 5.

5. Uncertainty Estimation

5.1. Bayesian Approach

The weighted least squares solution of Equation 13 is the trajectory for which the observed TOF and pre- t_0 pseudo speeds are the most likely, that is, the maximum likelihood solution. It is particularly important to characterize the reliability of this solution. In this section, we propagate the uncertainties from the measurements to the output trajectory and speed.

Approximate confidence intervals can be obtained by linearization of the cost function around the optimum solution. However, as we have illustrated in Balis et al. (2023), the CW forward scatter trajectory reconstruction

without interferometry is strongly ill-conditioned. This means that the sensitivity of the solution to errors in the observed inputs is very high. As a consequence, the cost function of Equation 13 often exhibits “flat minima,” which means that several solutions are almost as good as each other. In that case, it is difficult to select a single optimum solution and computing accurate uncertainties by linearization can be impossible.

For these reasons, we prefer to work in a Bayesian framework. Bayes' theorem writes:

$$P(m|D) = \frac{P(D|m)P(m)}{\int P(D|m')P(m')dm'}, \quad (15)$$

where $|$ is a conditional probability, m is the solution vector ($X_0, Y_0, Z_0, V_x, V_y, V_z$), and D is the observation vector made of the TOF and the pre- t_0 pseudo speeds.

In this framework, the solution is not deterministic but has instead a probability distribution $P(m|D)$ named the posterior distribution. Moreover, we can incorporate prior information about the solution through $P(m)$, which can either come from physical properties or previous experience with the problem at hand. The remaining terms are the likelihood function $P(D|m)$ and a normalization constant in the denominator.

While we work with probability distributions, it often is helpful for interpretation purposes to isolate a single solution from the posterior $P(m|D)$. A common approach is the selection of the solution which maximizes the posterior distribution. Such a solution is named maximum a posteriori (MAP). In the case of an uninformative prior, we have $P(m|D) \propto P(D|m)$ and the posterior distribution is precisely the likelihood function. It is possible to show (Aster et al., 2019) that, when the prior is uninformative and the data are independent and normally distributed, the MAP solution is precisely the solution of Equation 13.

In our case, we stay consistent with the developments presented in Balis et al. (2023) and we introduce additional constraints on the altitude and the velocity on the trajectory, both during the reconstruction of the trajectory and the determination of its uncertainties. That corresponds to using a rectangular prior which is equal to 1 within the physical bounds of the model, and 0 outside.

Following the developments presented in Kastinen and Kero (2022), and the assumption of independent measurements, our likelihood function can be expressed as:

$$P(D|m) = \prod_i p_{\Delta t}(\Delta t_{i,obs}|\Delta t_{i,model}) \prod_j p_{pt0}(v_{j,pt0}|v_{j,model}), \quad (16)$$

where \prod_i indicates a product on all the stations i .

By using the assumption of Gaussian measurement distributions, we can define the log-likelihood as:

$$\log P(D|m) = C - \frac{1}{2} \sum_{i=1}^n \left(\frac{\Delta t_{i,obs} - \Delta t_{i,model}}{\hat{\sigma}_{\Delta t_{i,obs}}} \right)^2 - \frac{1}{2} \sum_{j=1}^m \left(\frac{v_{j,pt0} - v_{j,model}}{\hat{\sigma}_{v_{j,pt0}}} \right)^2, \quad (17)$$

where C is a normalization constant.

It is important to note that there is a proportionality between the log-likelihood and the cost function of Equation 13. This relationship is particularly useful because it allows us to use the cost function in order to sample the posterior distribution.

5.2. Markov Chain Monte Carlo (MCMC)

Markov Chain Monte Carlo (MCMC) methods are a powerful tool to sample from a probability distribution. In particular, they can be used to characterize the properties of the posterior distribution of a nonlinear inverse problem within a Bayesian framework.

Markov Chains are designed so that their equilibrium distribution is equal to the probability distribution from which they are sampled. As a result, as the length of the chain increases, the distribution created by the chain should converge to the target distribution, in this case the posterior. To do so, using the proportionality between

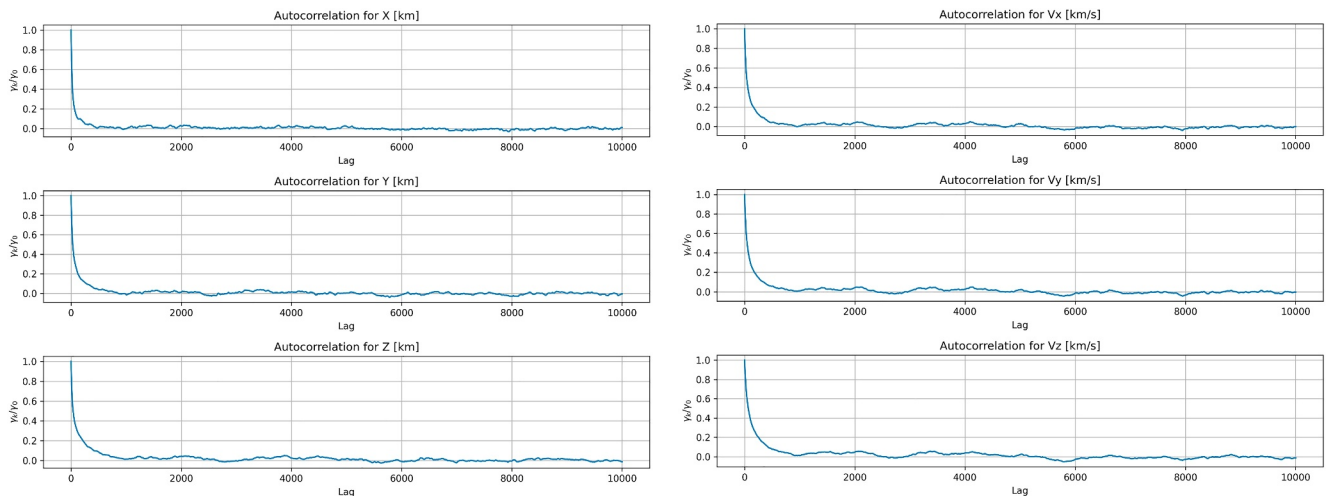


Figure 9. The normalized autocorrelation function $\frac{\gamma_k}{\gamma_0}$ for a Markov-Chain Monte Carlo chain at different lags k for each of the six observables per trajectory solution.

posterior and likelihood, we sample from the log-likelihood distribution given in Equation 17. As the expression is symmetric between observed and modeled parameters, we can simply evaluate the uncertainties in the denominators once and keep them fixed throughout the MCMC process.

We base our developments on the original work carried out by Kastinen and Kero (2022) for the computation of uncertainties on meteor head echo parameters. In particular, we use a method called Single Component Adaptive Metropolis-Hastings (SCAM), presented by Haario et al. (2005).

SCAM is inspired from the Metropolis-Hastings algorithm. The latter requires two distributions: a proposal distribution that determines in what zones the posterior should be preferably sampled, and an acceptance distribution which ensures that the condition of local balance is respected, that is, that the Markov Chain effectively converges toward the posterior distribution (Hastings, 1970).

While the proposal distribution can be selected freely, a natural choice is to use a multivariate normal distribution. The given covariances and variances of the proposal distribution can be obtained in two different ways. The first option is to start from a scaled identity matrix and then to progressively update the covariances and variances thanks to the samples of the Markov Chain. The second option is to take the linear covariance matrix as the proposal matrix and to set it fixed throughout the building of the chain. This latter option is preferred as we observe that it increases the convergence rate.

The correlation between successive samples is one of the great challenges related to MCMC. To quantify this phenomenon, we look at the autocorrelation function γ , which quantifies the dependence between successive samples in the Markov Chain. We give an example of the autocorrelation function obtained at increasing lags k for a given MCMC run in Figure 9. In that case, we can see that the autocorrelation reaches 0 after a lag of about 1,000 samples. This means that the sample n and the sample $n + 1000$ are decorrelated. In order to adequately explore the posterior distribution while limiting the computational cost of the process, we choose a Markov Chain length of 300,000 samples.

One complicating aspect of MCMC is the bias introduced by the initial solution from which the Markov Chain begins. In some cases, this can cause the algorithm to miss the high-probability regions of the log-likelihood. To address this, the common strategy is to allow the algorithm to “burn in,” a phase during which samples are generated but not stored. The duration of the burn-in phase is typically set to the lag after which autocorrelation drops to zero. In our case, we benefit from the solver's ability to provide the MAP solution to the trajectory problem, which, by definition, is the most likely solution. As a result, we set the initial sample of the Markov Chain to be the solution of Equation 13 and bypass the burn-in phase.

Table 1
CAMS-Measured Information Used for Solver Validation

Date	Time (UTC)	No.	$V_{\infty, \text{CAMS}}$ [km/s]	a_1 [km/s ²]	a_2 [s ⁻¹]	$Z_{0, \text{CAMS}}$ [km]	ϕ_{CAMS} [°]	θ_{CAMS} [°]
29-07-2020	23:14:00	79	41.96 ± 0.07	0.070 ± 0.006	3.408 ± 0.047	97.46	−17.39	128.22
29-07-2020	23:36:28	105	41.83 ± 0.09	0.068 ± 0.004	4.049 ± 0.092	100.21	−17.80	118.74
30-07-2020	00:51:27	188	29.95 ± 0.02	0.102 ± 0.002	2.017 ± 0.027	92.62	−10.63	88.91
30-07-2020	22:07:59	477	61.36 ± 0.02	0.003 ± 0.001	8.402 ± 0.043	110.03	−30.13	−131.75
30-07-2020	23:03:23	532	43.51 ± 0.12	0.226 ± 0.007	3.206 ± 0.134	92.17	−15.82	130.17
23-03-2022	00:44:00	92	63.62 ± 0.10	0.031 ± 0.003	5.493 ± 0.149	103.82	−24.69	163.90
27-04-2022	22:28:05	39	40.16 ± 0.01	5.031 ± 0.001	0.465 ± 0.002	102.46	−17.54	136.86
27-04-2022	23:07:25	49	39.13 ± 0.26	0.049 ± 0.010	8.447 ± 0.191	92.30	−19.63	115.21
31-01-2025	20:33:55	57	24.58 ± 0.02	0.557 ± 0.004	1.966 ± 0.018	95.36	−24.47	128.17
31-01-2025	23:36:28	166	35.45 ± 0.84	0.040 ± 0.021	3.795 ± 0.289	96.81	−25.86	136.62

Note. No. refers to the trajectory identification number from the CAMS data set. $V_{\infty, \text{CAMS}}$ represents the pre-atmospheric velocity of the meteoroid in km/s with its associated uncertainty. a_1 and a_2 are the deceleration components as presented in Equation 18, with their respective uncertainties. The last three columns are parameters indirectly retrieved from the CAMS trajectory: the altitude of the reference specular point $Z_{0, \text{CAMS}}$, the radiant elevation angle ϕ_{CAMS} and the radiant azimuth angle θ_{CAMS} .

6. Comparison With Optical Trajectories

In order to validate our novel implementations, we compare our trajectory reconstruction results with optical trajectories given by the CAMS-BeNeLux network (Jenniskens et al., 2016). At the time of writing, the CAMS network in the Benelux consists of more than 110 cameras that cover the sky above Belgium, the Netherlands, Luxembourg and part of Germany.

Initially introduced by Whipple and Jacchia (1957) and Jacchia et al. (1967), CAMS uses an exponential deceleration model:

$$V(t) = V_{\infty} - |a_1 a_2| \exp(a_2 t), \quad (18)$$

where $t = 0$ corresponds to the timing of the first recorded optical detection of the trail. V_{∞} is the pre-atmospheric speed and a_1 and a_2 are two deceleration parameters.

In Balis et al. (2023), we studied 10 trajectories from 2 consecutive nights of 29–31 July 2020. This set was determined through geometrical constraints, that is, we verified that enough BRAMS specular points were in the altitude range of 80–120 km, and through kinematic constraints on the speed, that is, we imposed that the meteoroid would travel at speeds between 11 and 72 km/s. We also required the Humain interferometer to be one of the receiving stations.

For this validation, while we maintain the same geometrical and kinematic constraints, we no longer require the Humain interferometer to be one of the receivers as we want to test our novel algorithm without interferometry. This added flexibility allows us to analyze a broader range of trajectories with more diverse geometries.

We also introduce an additional constraint based on the CAMS deceleration model. Zero deceleration values can often be attributed to rounding during output formatting, as extremely small values may be rounded down to zero. However, CAMS data files provide deceleration information up to 3 significant digits past the decimal. Moreover, a_1 values are usually in the range 1–100 km/s² (median precision of 0.85 km/s²) and the a_2 parameter has a median value of 1.21/s with an error proportional to the one in a_1 (Jenniskens et al., 2011). Consequently, we only consider trajectories whose a_1 and a_2 parameters are significantly greater than zero and whose corresponding uncertainties σ_{a_1} and σ_{a_2} are also greater than zero.

As a result, we select five of the ten trajectories analyzed in Balis et al. (2023) and introduce five new ones, as shown in Table 1. In our previous study, we consistently chose Humain as the reference station. In the current analysis, however, the reference station is chosen as the first station along the trajectory that provides a usable pre- t_0 speed measurement.

Table 2
Comparison of Maximum a Posteriori Belgian RADio Meteor Stations Reconstructions and CAMS Trajectories

No.	TOF	Pre- t_0	$\frac{V_{\text{tof}} - V_{\text{CAMS}}}{V_{\text{CAMS}}} [\%]$	$\frac{V_{\text{pt0}} - V_{\text{CAMS}}}{V_{\text{CAMS}}} [\%]$	$\Delta Z_{0,\text{tof}} [\text{km}]$	$\Delta Z_{0,\text{pt0}} [\text{km}]$	$\Delta \alpha_{\text{tof}} [^\circ]$	$\Delta \alpha_{\text{pt0}} [^\circ]$
79	17	10	-15.93	-3.26	9.73	2.06	16.24	3.73
105	11	3	-9.04	-1.20	18.45	8.41	11.77	2.04
188	7	3	-5.60	-2.00	6.53	3.51	9.56	2.45
477	16	10	-28.56	-1.47	2.91	9.81	21.62	2.70
532	7	2	-11.89	-4.42	2.11	0.27	12.35	4.21
92	18	8	-10.30	-1.53	13.19	2.29	12.50	2.59
39	6	4	-4.20	-0.98	7.52	8.69	0.13	2.91
49	7	1	38.80	-8.42	27.70	7.31	98.02	2.55
57	21	13	-1.27	-2.33	0.07	1.03	6.24	4.48
166	14	13	-15.85	-5.65	14.44	0.60	11.17	0.46

Note. The second and third columns give the number of receivers which produce echos exploitable for times of flight (TOF) and pre- t_0 speed extraction per meteor. The next columns provide errors in terms of relative speed, absolute reference specular point altitude as well as inclination angle, both for the method using the times of flight only (subscript tof) and the approach complementing the times of flight with the pre- t_0 speeds (subscript pt0).

We first verify our reconstruction results obtained with TOF only, and with a combination of TOF and pre- t_0 speeds, as illustrated in Table 2. These results have been obtained by comparing the MAP output of the solver with the CAMS solution. The CAMS velocity used for comparison is taken at $t = 0$ while the altitude is compared at the reference specular point. The errors in relative speed, altitude, and inclination angle highlight the advantages of using pre- t_0 speed data for the trajectory reconstruction. Examination of the table shows that:

- The absolute speed errors are significantly reduced when combining TOF data with pre- t_0 speeds, being systematically under 10%, and under 5% for most cases. The mean speed error with pre- t_0 information is 3.13%.
- The benefit on the altitude determination is moderate, as it is improved in 7 cases, and deteriorated in 3 cases. A significant advantage of the addition of the pre- t_0 information is that the altitude is always constrained within 10 km. The mean altitude error is 4.40 km.
- The inclination angle error shows the most notable improvement, with a mean error of 2.81° . In extreme cases, such as No. 49, the error in inclination angle is reduced by over 95° thanks to the pre- t_0 information at only one station, showing the significant benefit of incorporating phase data.

While we give point estimates of the error in the solution in Table 2, the Bayesian framework describes the solution as a probability distribution. As a result, we can extract scatter matrices coming from the MCMC chain to better understand the behavior of the solution. An example is given for Trajectory 79 in Figure 10, using both TOF and pre- t_0 phases.

The width of the histograms in the diagonal plots of Figure 10 gives us an indication of the uncertainty in the six parameters of the solution. The off-diagonal plots illustrate the correlations between different parameters. In this case, it appears that the position parameters X_0 , Y_0 and Z_0 are quite decorrelated, as their scatter plots are almost circular. However, there is a strong linear correlation between the different velocity components V_x , V_y and V_z , which is another proof of the ill-conditioning of the trajectory reconstruction problem without interferometry. There is also some moderate correlation between the velocity components and the position parameters.

For the same trajectory 79, we plot the density matrix for several outputs of interest in Figure 11: the radiant elevation angle ϕ , the radiant azimuth angle θ , the altitude of the reference specular point Z_0 and the speed V . The off-diagonal plots show the relative independence of the azimuth from the other parameters. On the other hand, there are significant correlations between the elevation angle, the altitude and the speed. These plots also highlight the nonlinearity of the trajectory reconstruction, as evidenced by the non-normality of the distributions, particularly for Z_0 .

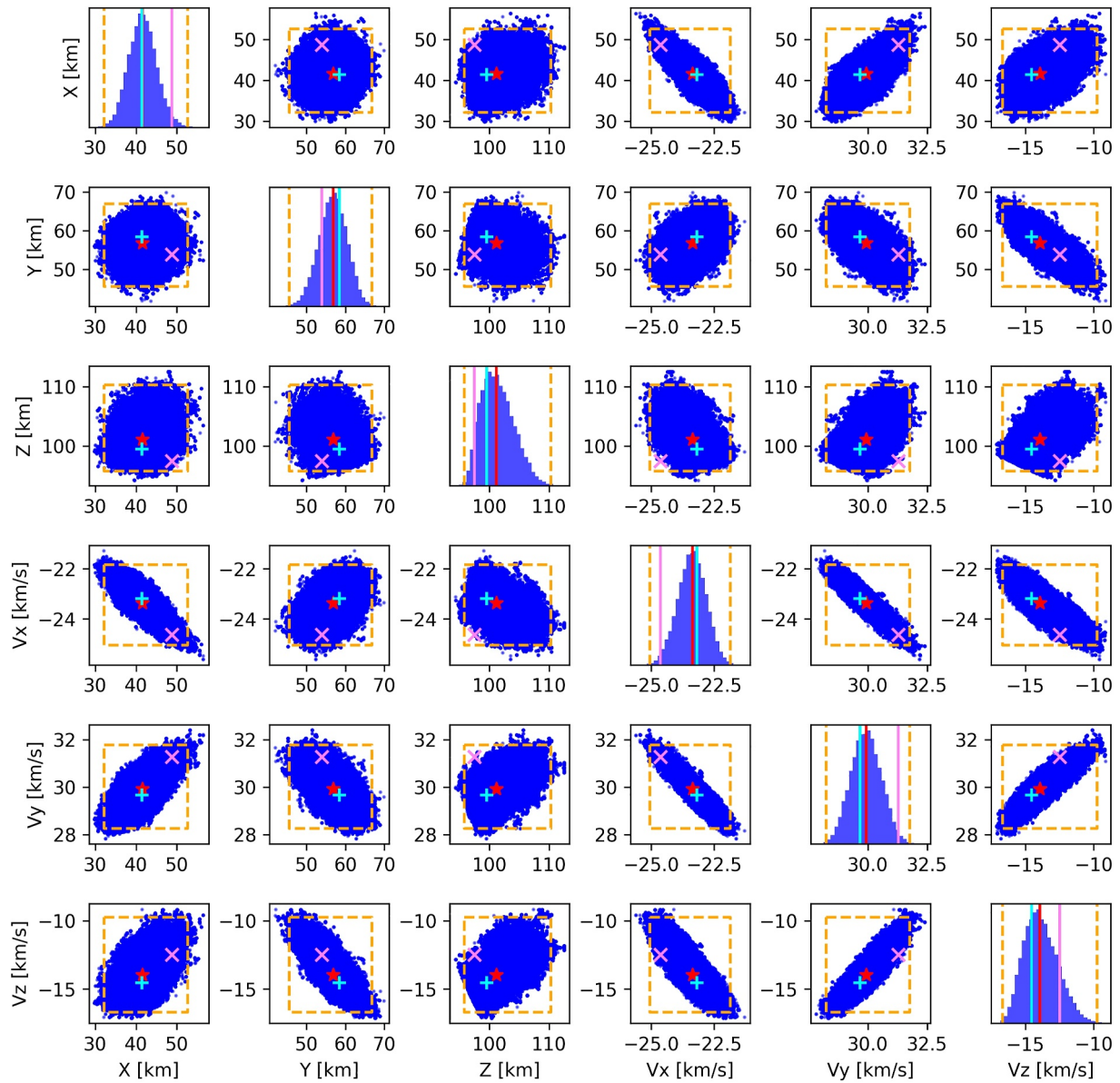


Figure 10. Scatter matrix for the parameters of trajectory 79 obtained with 300,000 samples (in blue) of the Single Component Adaptive Metropolis-Hastings algorithm applied with the log-likelihood given in Equation 17. The cyan plus/line is the solution returned by the solver. The red star/line is the median of the posterior distribution. The violet cross/line is the CAMS solution. The dashed orange lines show the 3σ confidence intervals.

In some cases, the CAMS solution may appear outside the 3σ bounds of the BRAMS posterior. However, it is important to remember that CAMS solutions also have associated error distributions, and the depicted violet crosses in Figures 10 and 11 are only the center points of these distributions. Therefore, the underlying BRAMS and CAMS distributions always overlap to some extent, allowing for a meaningful comparison. The determination of CAMS uncertainties is discussed by Jenniskens et al. (2011).

Since we now have access to probability distributions thanks to the MCMC method, we can define uncertainties by the use of credible intervals. In particular, we report a measure of $+\sigma$ and $-\sigma$ using respectively the distance between the 84th percentile and the median, and between the median and the 16th percentile. The results are given in Table 3.

The uncertainties determined by the Markov Chain appear to be physically reasonable; they increase as the difference with the CAMS solution grows. It appears that the uncertainty bounds on altitude and elevation angle

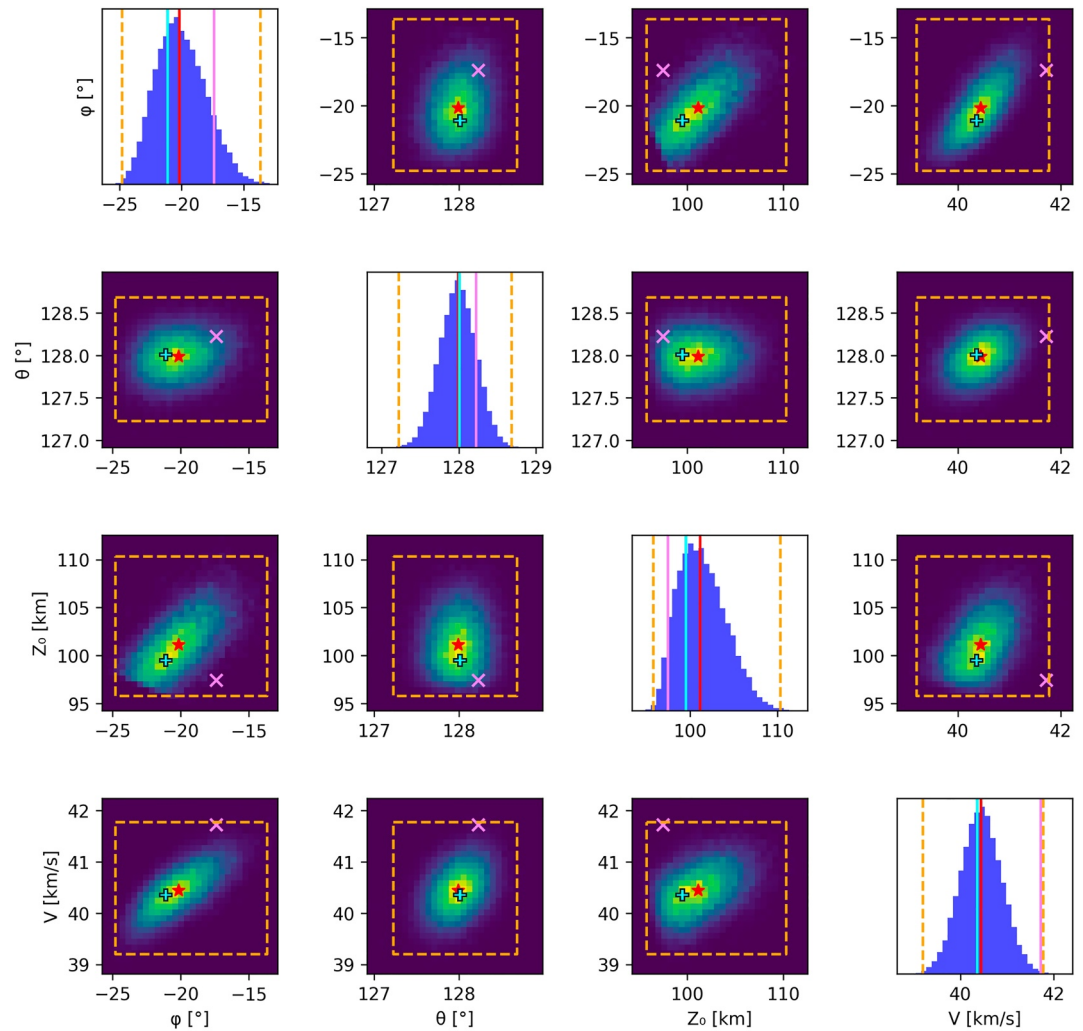


Figure 11. Density matrix for the same Markov Chain as in Figure 10. The parameters displayed are the elevation angle ϕ and the azimuth angle θ of the velocity vector, the altitude Z_0 of the reference specular point and the speed V of the meteoroid. The lines and markers are the same as in Figure 10, with the cyan plus signs additionally outlined in black to improve visibility.

are relatively wide. However, the azimuth angle is tightly determined, demonstrating the method's ability to capture horizontal trajectory components. More importantly, the speed is well constrained, which is essential for accurate orbit determination (Vida et al., 2018).

7. Conclusion and Perspectives

We have shown that the pre- t_0 phase technique when coupled with time of flight measurements improves meteoroid trajectory and speed reconstruction using forward-scatter radio systems. By leveraging phase information recorded prior to the specular reflection point, this method enhances speed estimations and, when integrated into a trajectory solver, contributes to a more robust determination of the meteoroid's path. One of the key benefits of this technique is that it allows for improved accuracy without requiring interferometry, thereby broadening the applicability of CW radio networks like BRAMS. The results obtained through comparisons with optical data of the CAMS-BeNeLux network confirm the efficiency of this approach, demonstrating notable improvements in speed and inclination estimates.

Given the nonlinear and ill-conditioned nature of the inverse problem of trajectory reconstruction using multi-static forward scatter radio meteor measurements, performing uncertainty estimation using MCMC methods is crucial. The Bayesian framework implemented in this study allows for a more comprehensive characterization of

Table 3

Comparison Between the Reconstructions With Belgian RAdio Meteor Stations and With CAMS for the Same Parameters as Illustrated in Figure 11

No.	V [km/s]	V_{CAMS} [km/s]	Z_0 [km]	$Z_{0,\text{CAMS}}$ [km]	ϕ [°]	ϕ_{CAMS} [°]	θ [°]	θ_{CAMS} [°]
79	40.44 ^{+0.45} _{-0.43}	41.72	101.17 ^{+3.01} _{-2.58}	97.46	-20.18 ^{+2.27} _{-1.88}	-17.39	127.99 ^{+0.23} _{-0.24}	128.22
105	42.02 ^{+0.54} _{-0.75}	41.55	91.96 ^{+5.54} _{-5.22}	100.21	-9.16 ^{+5.01} _{-6.84}	-17.80	120.48 ^{+0.47} _{-0.49}	118.74
188	29.21 ^{+0.32} _{-0.35}	29.74	90.21 ^{+1.85} _{-1.96}	92.62	-13.11 ^{+2.62} _{-2.63}	-10.63	89.10 ^{+0.15} _{-0.15}	88.91
477	58.84 ^{+1.30} _{-1.65}	61.33	111.38 ^{+5.62} _{-8.81}	110.03	-34.83 ^{+1.49} _{-1.85}	-30.13	-132.46 ^{+0.13} _{-0.13}	-131.75
532	41.42 ^{+1.07} _{-0.93}	42.79	94.72 ^{+6.28} _{-4.79}	92.17	-18.92 ^{+2.43} _{-1.91}	-15.82	129.95 ^{+0.20} _{-0.22}	130.17
92	62.57 ^{+0.66} _{-0.65}	63.45	106.21 ^{+2.94} _{-2.83}	103.82	-26.75 ^{+1.89} _{-1.78}	-24.69	162.73 ^{+0.20} _{-0.21}	163.90
39	37.57 ^{+0.25} _{-0.38}	37.82	112.72 ^{+2.87} _{-5.86}	102.46	-21.46 ^{+4.41} _{-5.52}	-17.54	134.89 ^{+1.28} _{-1.30}	136.86
49	36.15 ^{+1.00} _{-1.18}	38.72	87.14 ^{+4.50} _{-3.23}	92.30	-10.67 ^{+6.11} _{-6.74}	-19.63	116.15 ^{+0.46} _{-0.50}	115.21
57	23.09 ^{+0.19} _{-0.18}	23.48	96.40 ^{+2.42} _{-1.65}	95.36	-26.49 ^{+2.55} _{-2.29}	-24.47	126.81 ^{+0.33} _{-0.31}	128.17
166	34.32 ^{+0.86} _{-0.77}	35.30	103.72 ^{+6.73} _{-4.44}	96.81	-24.09 ^{+1.65} _{-1.48}	-25.86	136.43 ^{+0.80} _{-0.81}	136.62

Note. The format of BRAMS solutions is given as $med^{+\sigma}_{-\sigma}$ where med is the median sample of the posterior distribution. $-\sigma$ and $+\sigma$ are determined from the corresponding distribution percentiles.

uncertainties by accounting for multiple plausible solutions. This ensures that the derived trajectory parameters are not only reliable but also accompanied by well-quantified confidence intervals.

While the pre- t_0 phase technique significantly enhances trajectory reconstruction, certain applications will still benefit from interferometry. Accurate altitude retrieval is particularly relevant for studying Mesosphere-Lower Thermosphere winds, where altitude biases could impact derived atmospheric dynamics. Integrating interferometric data with pre- t_0 information where available appears as a promising avenue to drive down the uncertainty in altitude determination.

Looking ahead, several improvements would further enhance this methodology. All the MAP speeds in Table 2 are lower than the CAMS speeds in $t = 0$. This systematic bias arises from the constant speed assumption used in this study. Incorporating a deceleration model, such as the exponential one used by CAMS, could improve speed estimation. However, this would also increase the problem's dimensionality, making convergence more challenging—particularly since the exponential model has proven difficult to fit (Egal et al., 2017). One might consider exploring various approaches, such as constant velocity, linear and exponential deceleration, and selecting the one that best fits the data. Additionally, estimating initial speed from optical lag estimates using an iterative approach, such as that proposed in (Vida et al., 2019), might improve initial velocity estimation.

To further enhance the accuracy of trajectory reconstructions, additional inputs could be incorporated into the solver. One possibility is to supplement the cost function of Equation 13 with information from the FT. This approach was recently analyzed and refined for fragmentation analysis using CMOR data (Balis et al., 2024). One of its most notable byproducts is the introduction of constraints between the meteoroid's range and velocity, which would further improve the conditioning of the trajectory reconstruction process.

A direct outcome of the improved trajectory reconstruction is a straightforward path to more accurate orbit determination. Future coupling of trajectory solutions produced from BRAMS using this approach with existing tools, such as the WMPL package by Vida et al. (2019) or the REBOUND N-body integrator by Rein and Liu (2012), will be implemented. These developments will together contribute to a better assessment of impact risk with spacecraft, improved characterization of atmospheric dynamics, as well as a deeper understanding of meteoroid origins and their link to parent bodies in the Solar System.

Data Availability Statement

All code developed during this project is openly available as part of the PyBRAMS package, hosted at <https://gitlab.aeronomie.be/ae/brams/pybrams>. The version 0.1.1 of the PyBRAMS package, used for the generation of

the results presented in this paper, is preserved at <https://doi.org/10.5281/zenodo.15174740>, available via Creative Commons Attribution 4.0 International (Balis, 2025).

Acknowledgments

Joachim Balis is funded by the Solar-Terrestrial Center of Excellence (STCE). The BRAMS network is supported in part by STCE, and by the Services and Operability of the BRAMS nETwork (SORBET) project (Contract No. RT/23/SORBET). BRAMS is an active Pro-Am collaboration, and we thank all operators for hosting the receiving stations. PGB acknowledges funding support for this project through NASA co-operative agreement 80NSSC24M0060.

References

- Anciaux, M., Lamy, H., Martinez Picar, A., Calders, S., Calegario, A., Ranvier, S., & Verbeeck, C. (2020). The brams receiving station v2.0. In U. Pajer, J. Rendtel, M. Gyssens, & C. Verbeeck (Eds.), *Proceedings of the international meteor conference* (pp. 39–42).
- Aster, R. C., Borchers, B., & Thurber, C. H. (2019). Chapter four—Tikhonov regularization. In R. C. Aster, B. Borchers, & C. H. Thurber (Eds.), *Parameter estimation and inverse problems* (3rd ed., 3rd ed. ed., pp. 93–134). Elsevier. <https://doi.org/10.1016/B978-0-12-804651-7.00009-2>
- Baggaley, W. (2009). Meteoric ionization: The interpretation of radar trail echoes. *Radio Science Bulletin*, 329, 6–20.
- Baggaley, W. J., Bennett, R. G. T., & Taylor, A. D. (1997). Radar meteor atmospheric speeds determined from echo profile measurements. *Planetary and Space Science*, 45(5), 577–583. [https://doi.org/10.1016/S0032-0633\(97\)00023-8](https://doi.org/10.1016/S0032-0633(97)00023-8)
- Baggaley, W. J., & Grant, J. (2005). Techniques for measuring radar meteor speeds. In *Modern meteor science an interdisciplinary view* (pp. 601–615). Springer Netherlands. https://doi.org/10.1007/1-4020-5075-5_56
- Balis, J. (2025). Pybrams package (version 0.1.1) [Software]. Zenodo. <https://doi.org/10.5281/zenodo.15174739>
- Balis, J., Brown, P., Lamy, H., & Jehin, E. (2024). Fresnel holography for radio characterization of meteoroid fragmentation. *Copernicus Meetings*
- Balis, J., Lamy, H., Anciaux, M., & Jehin, E. (2023). Reconstructing meteoroid trajectories using forward scatter radio observations from the brams network. *Radio Science*, 58(6), e2023RS007697. <https://doi.org/10.1029/2023RS007697>
- Campbell, L., & Elford, W. (2006). Accuracy of meteoroid speeds determined using a fresnel transform procedure. *Planetary and Space Science*, 54(3), 317–323. <https://doi.org/10.1016/j.pss.2005.12.016>
- Carrillo-Sánchez, J. D., Nesvorný, D., Pokorný, P., Janches, D., & Plane, J. M. C. (2016). Sources of cosmic dust in the earth's atmosphere. *Geophysical Research Letters*, 43(23), 11979–11986. <https://doi.org/10.1002/2016GL071697>
- Ceplecha, Z. (1987). Geometric, dynamic, orbital and photometric data on meteoroids from photographic fireball networks. *Bulletin of the Astronomical Institutes of Czechoslovakia*, 38, 222–234.
- Ceplecha, Z., Borovička, J., Elford, W. G., Revelle, D. O., Hawkes, R. L., Porubčan, V., & Šimek, M. (1998). Meteor phenomena and bodies. *Space Science Reviews*, 84(3–4), 327–471. <https://doi.org/10.1023/A:1005069928850>
- Cervera, M. A., Elford, W. G., & Steel, D. I. (1997). A new method for the measurement of meteor speeds: The pre-to phase technique. *Radio Science*, 32(2), 805–816. <https://doi.org/10.1029/96RS03638>
- Egal, A., Gural, P. S., Vaubaillon, J., Colas, F., & Thuillot, W. (2017). The challenge associated with the robust computation of meteor velocities from video and photographic records. *Icarus*, 294, 43–57. <https://doi.org/10.1016/j.icarus.2017.04.024>
- Elford, W. G. (2004). Radar observations of meteor trails, and their interpretation using fresnel holography: A new tool in meteor science. *Atmospheric Chemistry and Physics*, 4(4), 911–921. <https://doi.org/10.5194/acp-4-911-2004>
- Elford, W. G., & Campbell, L. (2001). Effects of meteoroid fragmentation on radar observations of meteor trails. In B. Warmbein (Ed.), *Meteoroids 2001 conference* (Vol. 495, pp. 419–423).
- Ellyett, C. D., & Davies, J. G. (1948). *Velocity of meteors measured by diffraction of radio waves from trails during formation*. Nature Publishing Group.
- Haario, H., Saksman, E., & Tamminen, J. (2005). Componentwise adaptation for high dimensional MCMC. *Computational Statistics*, 20(2), 265–273. <https://doi.org/10.1007/BF02789703>
- Hansen, P. C. (1992). Analysis of discrete ill-posed problems by means of the l-curve. *SIAM Review*, 34(4), 561–580. <https://doi.org/10.1137/1034115>
- Hastings, W. K. (1970). Monte Carlo sampling methods using Markov chains and their applications. *Biometrika*, 57(1), 97–109. <https://doi.org/10.2307/2334940>
- Holdsworth, D. A., Elford, W. G., Vincent, R. A., Reid, I. M., Murphy, D. J., & Singer, W. (2007). All-sky interferometric meteor radar meteoroid speed estimation using the Fresnel transform. *Annales Geophysicae*, 25(2), 385–398. <https://doi.org/10.5194/angeo-25-385-2007>
- Jacchia, L., Verniani, F., & Briggs, R. E. (1967). An analysis of the atmospheric trajectories of 413 precisely reduced photographic meteors. *Smithsonian Contributions to Astrophysics*, 10, 1–139. <https://doi.org/10.5479/si.00810231.10-1.1>
- Jenniskens, P., Gural, P., Dynneson, L., Grigsby, B., Newman, K., Borden, M., et al. (2011). Cams: Cameras for Allsky meteor surveillance to establish minor meteor showers. *Icarus*, 216(1), 40–61. <https://doi.org/10.1016/j.icarus.2011.08.012>
- Jenniskens, P., Nénon, Q., Albers, J., Gural, P., Haberman, B., Holman, D., et al. (2016). The established meteor showers as observed by cams. *Icarus*, 266, 331–354. <https://doi.org/10.1016/j.icarus.2015.09.013>
- Jones, J., Brown, P., Ellis, K., Webster, A., Campbell-Brown, M., Krzeminski, Z., & Weryk, R. (2005). The Canadian meteor orbit radar: System overview and preliminary results. *Planetary and Space Science*, 53(4), 413–421. <https://doi.org/10.1016/j.pss.2004.11.002>
- Kastinen, D., & Kero, J. (2022). Radar analysis algorithm for determining meteor head echo parameter probability distributions. *Monthly Notices of the Royal Astronomical Society*, 517(3), 3974–3992. <https://doi.org/10.1093/mnras/stac2727>
- Kraft, D. (1988). A software package for sequential quadratic programming. *Wiss. Berichtswesen d. DFVLR*. Retrieved from <https://books.google.be/books?id=4rKaGwAACAAJ>
- Lamy, H., Anciaux, M., Ranvier, S., Calders, S., Gamby, E., Martinez Picar, A., & Verbeeck, C. (2015). Recent advances in the BRAMS network. In *International meteor conference mistelbach*. 171
- Mazur, M., Pokorný, P., Brown, P., Weryk, R. J., Vida, D., Schult, C., et al. (2020). Precision measurements of radar transverse scattering speeds from meteor phase characteristics. *Radio Science*, 55(10), e2019RS006987. <https://doi.org/10.1029/2019RS006987>
- McKinley, D. (1961). *Meteor science and engineering*. McGraw-Hill. Retrieved from <https://books.google.be/books?id=BSAIAQAIAAJ>
- Rao, R., & Lakshmi, R. (2021). Ranking of pareto-optimal solutions and selecting the best solution in multi- and many-objective optimization problems using r-method. *Soft Computing Letters*, 3, 100015. <https://doi.org/10.1016/j.socl.2021.100015>
- Rein, H., & Liu, S.-F. (2012). Rebound: An open-source multi-purpose n-body code for collisional dynamics. *A&A*, 537, A128. <https://doi.org/10.1051/0004-6361/201118085>
- Roy, A., Doherty, J. F., & Mathews, J. D. (2007). Analyzing radar meteor trail echoes using the fresnel transform technique: A signal processing viewpoint. *Earth, Moon, and Planets*, 101(1), 27–39. <https://doi.org/10.1007/s11038-007-9147-5>
- Soja, R. H., Grün, E., Strub, P., Sommer, M., Millinger, M., Vaubaillon, J., et al. (2019). Imem2: A meteoroid environment model for the inner solar system. *A&A*, 628, A109. <https://doi.org/10.1051/0004-6361/201834892>
- Vida, D., Brown, P. G., & Campbell-Brown, M. (2018). Modelling the measurement accuracy of pre-atmosphere velocities of meteoroids. *Monthly Notices of the Royal Astronomical Society*, 479(4), 4307–4319. <https://doi.org/10.1093/mnras/sty1841>

- Vida, D., Gural, P. S., Brown, P. G., Campbell-Brown, M., & Wiegert, P. (2019). Estimating trajectories of meteors: An observational Monte Carlo approach—I. Theory. *Monthly Notices of the Royal Astronomical Society*, 491(2), 2688–2705. <https://doi.org/10.1093/mnras/stz3160>
- Wang, Z., & Rangaiah, G. P. (2017). Application and analysis of methods for selecting an optimal solution from the pareto-optimal front obtained by multiobjective optimization. *Industrial & Engineering Chemistry Research*, 56(2), 560–574. <https://doi.org/10.1021/acs.iecr.6b03453>
- Weryk, R. J., & Brown, P. G. (2012). Simultaneous radar and video meteors—I: Metric comparisons. *Planetary and Space Science*, 62(1), 132–152. <https://doi.org/10.1016/j.pss.2011.12.023>
- Whipple, F. L., & Jacchia, L. G. (1957). Reduction methods for photographic meteor trails. *Smithsonian Contributions to Astrophysics*, 1, 183–206.
- Wislez, J.-M. (2006). Meteor astronomy using a forward scatter set-up. In C. Verbeeck & J.-M. Wislez (Eds.), *Proceedings of the radio meteor school* (pp. 84–106).